Inorganic Chemistry

Article

pubs.acs.org/IC

# Light-Driven Proton Reduction in Aqueous Medium Catalyzed by a Family of Cobalt Complexes with Tetradentate Polypyridine-Type Ligands

Lianpeng Tong,[†] Andrew Kopecky,[†] Ruifa Zong,[†] Kevin J. Gagnon,[§] Mårten S. G. Ahlquist,*[,‡] and Randolph P. Thummel*[,†]

[†]Department of Chemistry, University of Houston, 112 Fleming Building, Houston, Texas 77204-5003, United States

[‡]Division of Theoretical Chemistry & Biology, School of Biotechnology, KTH Royal Institute of Technology, 10691 Stockholm, Sweden

[§]Advanced Light Source, Lawrence Berkeley National Laboratory, 1 Cyclotron Rd., Berkeley, California 94720, United States

Supporting Information

**ABSTRACT:** A series of tetradentate 2,2′:6′,2″:6″,2‴-quaterpyridine-type ligands related to ppq (ppq = 8-(1″,10″-phenanthrol-2″-yl)-2-(pyrid-2′-yl)quinoline) have been synthesized. One ligand replaces the 1,10-phenanthroline (phen) moiety of ppq with 2,2′-bipyridine and the other two ligands have a 3,3′-polymethylene subunit bridging the quinoline and pyridine. The structural result is that both the planarity and flexibility of the ligand are modified. Co(II) complexes are prepared and characterized by ultraviolet−visible light (UV-vis) and mass spectroscopy, cyclic voltammetry, and X-ray analysis. The light-driven $H_2$-evolving activity of these Co complexes was evaluated under homogeneous aqueous conditions using $[Ru(bpy)_3]^{2+}$ as the photosensitizer, ascorbic acid as a sacrificial electron donor, and a blue light-emitting diode (LED) as the light source. At pH 4.5, all three complexes plus $[Co(ppq)Cl_2]$ showed the fastest rate, with the dimethylene-bridged system giving the highest turnover frequency (2125 $h^{-1}$). Cyclic voltammograms showed a significant catalytic current for $H_2$ production in both aqueous buffer and $H_2O$/DMF medium. Combined experimental and theoretical study suggest a formal Co(II)-hydride species as a key intermediate that triggers $H_2$ generation. Spin density analysis shows involvement of the tetradentate ligand in the redox sequence from the initial Co(II) state to the Co(II)-hydride intermediate. How the ligand scaffold influences the catalytic activity and stability of catalysts is discussed, in terms of the rigidity and differences in conjugation for this series of ligands.

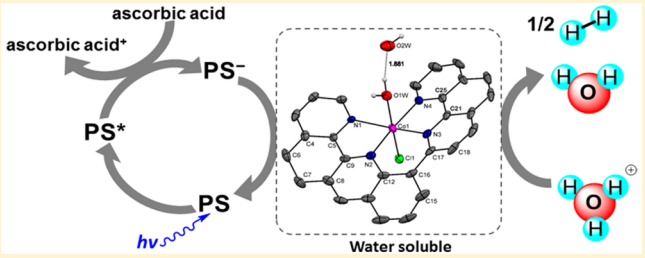


## INTRODUCTION

The use of hydrogen as a fuel represents an appealing solution to the problems associated with the combustion of fossil fuels.[1,2] Currently hydrogen is mainly derived from the thermal cracking of low-molecular-weight hydrocarbons. This process is both energetically impractical and dependent on a fossil fuel. An ideal source of hydrogen would result from the decomposition of water into its elements using the energy derived from sunlight,[3,4] which is a process often referred to as artificial photosynthesis.[5,6] Water decomposition can be regarded as the combination of two individual half-reactions: water oxidation and proton reduction.

water oxidation:

$$H_2O \rightarrow \frac{1}{2}O_2 + 2H^+ + 2e^-$$

proton reduction:

$$2H^+ + 2e^- \rightarrow H_2$$

Efficient catalysts are required for the implementation of either process.[7−9] Early investigations on proton reduction catalysts (PRCs) relied on precious metals such as platinum and rhodium.[10−12] More recent studies have revealed that a variety of Earth-abundant metal-based complexes are active as PRCs.[13−15] In this regard, cobalt complexes, coordinated to imine or pyridine-type ligands, have drawn attention, because of the accessibility of cobalt hydride species such as Co(III)−H or Co(II)−H.[15−23]

Tetradentate macrocyclic imine/oxime ligands have been studied as effective platforms to support a cobalt center for photocatalytic and electrocatalytic proton reduction.[24−30] These cobalt PRCs often feature square-planar equatorial ligand scaffolds with open axial coordination sites. Most of them, however, only function well in nonaqueous media with strong organic acids acting as the proton source. Meanwhile, the imine or oxime moieties in the equatorial ligand may be

Received: April 23, 2015
Published: July 27, 2015





DOI: 10.1021/acs.inorgchem.5b00915
Inorg. Chem. 2015, 54, 7873−7884

destroyed by hydrogenation or hydrolysis that can occur under the acidic conditions.[26,29] In contrast, polypyridyl ligands are tolerant to both aqueous acid and base conditions. Furthermore, the binding cavity can be tailored to accommodate various transition-metal ions. The interest in employing polypyridyl ligands for proton reduction originates from early findings that $[Co(bpy)_3]^{2+}$ (bpy = 2,2′-bipyridine) served as a precatalyst for light-driven $H_2$ evolution.[31,32] A turnover number (TON) of 74 (based on the catalyst) has been achieved by a photocatalytic $H_2$-evolving system consisting of $[Co(bpy)_3]^{2+}$, an iridium sensitizer, and triethanolamine.[33] Because of the equilibrium in aqueous environment between $[Co(bpy)_3]^{2+}$ and $[Co(bpy)_2]^{2+}$, the bis-bipyridine species $[Co(bpy)_2]^{2+}$ or $[Co(bpy)_2(OH_2)_2]^{2+}$ may play the role of an authentic catalyst.[34] This conjecture is supported by the discovery that $[Co(PY4)(CNCH_3)_2]^{2+}$ (PY4 = 2-bis(2-pyridyl)(methoxy)methyl-6-pyridylpyridine), which contains four pyridyl donors and two labile acetonitrile at *cis* positions serves as an effective electrocatalytic PRC.[35] Lau and coworkers recently found that *trans*-$[Co(qpy)(OH_2)_2]^{2+}$ (qpy = 2,2′:6′,2″:6″,2‴-quaterpyridine) is a more robust catalyst toward photocatalytic proton reduction than $[Co(bpy)_2]^{2+}$.[36] The cobalt quaterpyridine complex remains active for 50 h under irradiation and drives more than 1000 turnovers of $H_2$ generation. However, the catalytic $H_2$-evolving rate by $[Co(qpy)(OH_2)_2]^{2+}$ is not greater than that of $[Co(bpy)_3]^{2+}$.

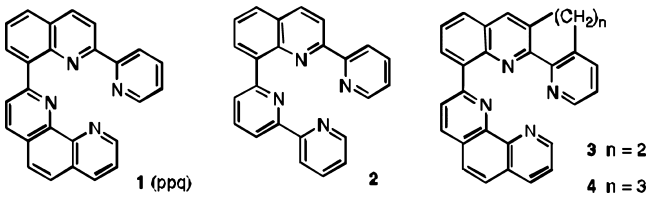


We have recently reported the synthesis of ppq (**1**, ppq = 8-(1″,10″-phenanthrol-2″-yl)-2-(pyrid-2′-yl)quinoline) as well as photocatalytic proton reduction by the $[Co(\mathbf{1})Cl_2]$ complex.[37] Combined with $[Ru(bpy)_3]^{2+}$ as a photosensitizer in buffered water (pH 4.0), $[Co(\mathbf{1})Cl_2]$ showed an initial turnover frequency (TOF) of 586 $h^{-1}$ per catalyst, which is significantly greater than the TOF of $[Co(bpy)_3]^{2+}$ or $[Co(qpy)(OH_2)_2]^{2+}$. Compared to bis-bipyridine and quaterpyridine, ppq has a less flexible and more conjugated backbone. Furthermore, because of the involvement of a 6-membered chelate ring, the binding cavity of ppq is smaller and a better fit for the size of Co(II) than quaterpyridine. These features of ppq may enhance catalytic proton reduction by providing (i) firm chelation between ppq and Co(II) and thus resisting distortion of the coordination geometry; (ii) $\pi$-electron delocalization over the entire ligand, facilitating reduction of the complex; and (iii) stability against ligand reduction or hydrolysis.

Aiming to better understand the activity of ppq-based cobalt PRCs, we prepared ligands **2**–**4**, which are closely related to the parent ppq. Ligands **1**–**4** are all tetradentate polypyridines in which the pyridines form an almost-square planar arrangement in what will become the equatorial plane of the complex. This arrangement is facilitated by the additional $sp^2$ carbon embodied by C8 of the central quinoline ring. When bound to a metal ion in a tetradentate fashion, these ligands will form three fused chelate rings containing five, six, and five atoms. We will refer to such systems as 5–6–5 chelators. By comparison, the cobalt quaterpyridine is a 5–5–5 chelator. Ligand **2**, consisting of four independent pyridines, contains three $\sigma$-bonds, providing greater flexibility than **1**, which has only two such bonds. In ligands **3** and **4** the 2-(pyrid-2′-yl)quinoline subunit has been tethered in the 3,3′ position by a dimethylene or trimethylene bridge that will control the dihedral angle between the pyridine and quinoline rings and also lend additional rigidity to the ligands that now have only one fully flexible C–C $\sigma$-bond. We also prepared $[Co(\mathbf{1})Br_2]$ having two bromide axial ligands rather than chlorides. In this paper, we will investigate the properties and catalytic performance of the series of cobalt catalysts bearing ligands **1**–**4** and probe mechanism of catalytic $H_2$ evolution.

## RESULTS

**Synthesis, Characterization, and Structure.** The preparation of ligand **1** and its Co(II) complex have been described previously.[37] Ligand **2** results from the Stille coupling of 6-tri-*n*-butylstannyl-2,2′-bipyridyl (**6**) with the bromoquinoline **5** that has been described earlier. The bridged ligands **3** and **4** were prepared in a similar manner from an initial Friedländer condensation of the pyridyl cycloalkanones **8a** and **8b** with 2-amino-3-bromobenzaldehyde to give **9a** and **9b**. The bromo-group was converted to acetyl through a Stille-type coupling with 1-ethoxyvinyl tri-*n*-butylstannane, followed by hydrolysis of the resulting vinyl ether. A second Friedländer condensation with 8-aminoquinoline-7-carbaldehyde provided the bridged ligands **3** and **4**. A schematic diagram detailing the synthesis of ligands **2**, **3**, and **4** is presented in Scheme 1. Ligands **1**–**4** have

**Scheme 1. Synthesis of 2, 3, and 4**

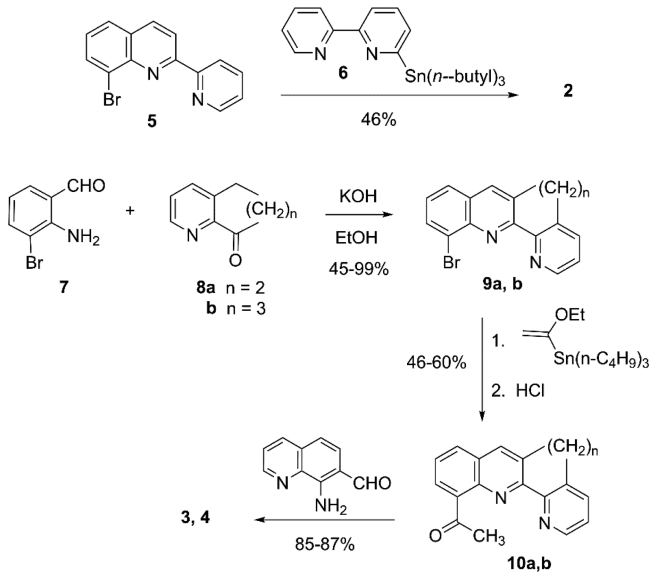


been characterized by $^1H$ and $^{13}C$ NMR (see Figures S1–S14 in the Supporting Information). The corresponding Co(II) complexes were prepared by treating **1**–**4** with $CoCl_2 \cdot 6H_2O$ or $CoBr_2$ in $MeOH/CHCl_3$ under aerobic conditions. The resulting cobalt complexes often are not soluble in the $MeOH/CHCl_3$ solvent and readily precipitate from the reaction solution. These complexes are paramagnetic and thus their proton NMR spectra were poorly defined. The complexes were spectroscopically characterized by UV-vis spectrometry, ESI mass spectrometry (see Figure S15 in the Supporting Information), and elemental analysis.

Two $[Co(\mathbf{2})Cl_2]$ molecules were observed in each asymmetric unit of its crystal (Figure S16 in the Supporting


DOI: 10.1021/acs.inorgchem.5b00915
Inorg. Chem. 2015, 54, 7873–7884

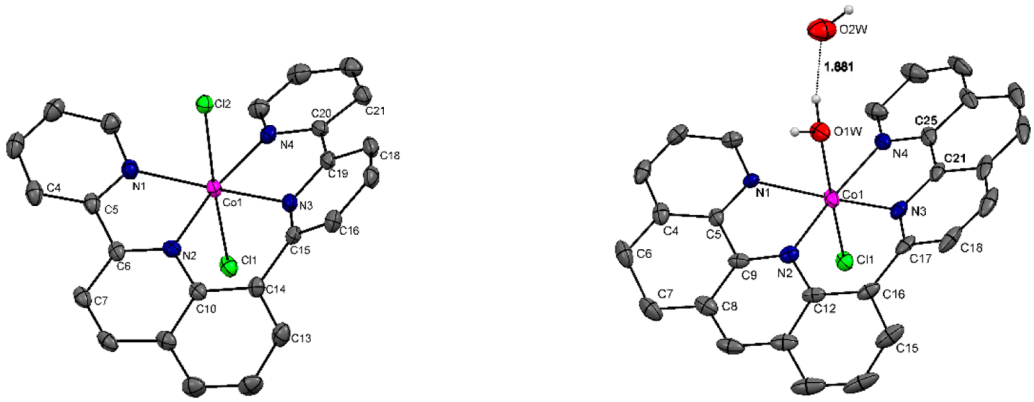


**Figure 1.** Thermal ellipsoid plot representations of crystal structures of $[Co(\mathbf{2})Cl_2]$ and $[Co(\mathbf{3})(OH_2)Cl]Cl$ at 50% probability; nonpolar hydrogen atoms, noncoordinating $Cl^-$ and fractional solvent molecules are omitted for clarity. [Color code: magenta, cobalt; blue, nitrogen; red, oxygen; dark gray, carbon; green, chlorine; and light gray, hydrogen.] The entire asymmetric unit of $[Co(\mathbf{2})Cl_2]$ contains two full molecules, which are displayed in the Supporting Information. The minor position of $[Co(\mathbf{3})(OH_2)Cl]Cl$ due to disorder is omitted.

**Table 1. Selected Bond Distances, Bond Angles, and Dihedral Angles for $[Co(\mathbf{2})Cl_2]$ and $[Co(\mathbf{3})(OH_2)Cl]Cl$**

| $[Co(\mathbf{2})Cl_2]$[a] | | $[Co(\mathbf{3})(OH_2)Cl]Cl$[b] | |
|---|---|---|---|
| **Bond Lengths (Å)** | | | |
| Co1−Cl1 | 2.4497(8) | Co1−Cl1 | 2.4140(4) |
| Co1−Cl2 | 2.5406(8) | Co1−O1W | 2.1950(11) |
| Co1−N1 | 2.089(2) | Co1−N1 | 2.146(5) |
| Co1−N2 | 2.097(2) | Co1−N2 | 2.060(8) |
| Co1−N3 | 2.060(2) | Co1−N3 | 2.011(3) |
| Co1−N4 | 2.099(2) | Co1−N4 | 2.141(2) |
| **Bond Angles (deg)** | | | |
| Cl1−Co1−Cl2 | 176.37(3) | Cl1−Co1−O1W | 171.20(3) |
| N1−Co1−N4 | 110.34(9) | N1−Co1−N4 | 106.85(15) |
| N1−Co1−N2 | 78.85(9) | N1−Co1−N2 | 79.3(2) |
| N2−Co1−N3 | 92.05(9) | N2−Co1−N3 | 92.8 (2) |
| N3−Co1−N4 | 79.14(9) | N3−Co1−N4 | 80.68(10) |
| **Dihedral Angles (deg)** | | | |
| N1−C5−C6−N2 | 12.9(3) | N1−C5−C9−N2 | 12.3(17) |
| C10−C14−C15−N3 | 40.9(4) | C12−C16−C17−N3 | 25.5(4) |
| N3−C19−C20−N4 | 17.3(3) | N3−C21−C25−N4 | 2.3(4) |

[a]The entire asymmetric unit of $[Co(\mathbf{2})Cl_2]$ contains two full molecules, the key parameters of which are described in the Supporting Information. [b]The distances and angles for the minor phase due to disorder have been omitted.

Information). Bond lengths and angles in these two molecules are very similar, but their torsional angles are slightly different, because of the three C−C $\sigma$-bonds of ligand **2** (see Table S2 in the Supporting Information). The ligand scaffold of $[Co(\mathbf{2})Cl_2]$ seems flexible enough to twist itself, to some degree, while maintaining the coordination geometry of the cobalt core. The thermal ellipsoid plot representations of a selected $[Co(\mathbf{2})Cl_2]$ molecule as well as the crystal structure of $[Co(\mathbf{3})(OH_2)Cl]Cl$ molecule are displayed in Figure 1. Similar to the structure of $[Co(\mathbf{1})Cl_2]$ reported recently,[37] both Co complexes adopt a distorted octahedral geometry, of which selected geometric parameters are listed in Table 1. The $Cl^-$ could play a role of either an "L-type" ligand or a noncoordinating anion in the most stable solid state of this series of Co complexes. The structures of $[Co(\mathbf{1})Cl_2]$ and $[Co(\mathbf{2})Cl_2]$ indicate that both axial positions are occupied by $\eta^1$-$Cl^-$ ligand while $[Co(\mathbf{3})(OH_2)Cl]^+$ contains only one $\eta^1$-$Cl^-$ ligand, as well as an aqua ligand. This aqua ligand forms a hydrogen bond with a solvated water molecule providing a hydrogen bonding network that is expected if $[Co(\mathbf{3})(OH_2)Cl]^+$ is dissolved in an aqueous environment. An important structural feature among these complexes is a Co−Cl bond that is considerably longer (2.4−2.6 Å) than the Co−Cl bonds found in diimine or dioxime Co complexes (2.2−2.3 Å) and closer to the Co−Cl bond distance in $CoCl_2$ (2.44−2.51 Å).[38,39] The long Co−Cl bond lengths endow these bonds with more ionic than covalent character and may facilitate dissociation of a chloride ligand from the cobalt complex in a protic solvent such as water. All Co−N bond distances lie in a narrow range of 2.0−2.1 Å, regardless of whether the N-donor is part of a pyridine, phen, or quinoline moiety. This consistency indicates a similar cavity size for **1**−**4** when they form a complex with Co(II).

The binding cavities for $[Co(\mathbf{2})Cl_2]$ and $[Co(\mathbf{3})(OH_2)Cl]^+$ are quite similar to that observed for the analogous complex of ligand **1**. The four Co−N bonds are arranged to create three fused chelate rings that contain five or six atoms, hence the designation of 5−6−5 chelators. This metal binding region consists of three distinct domains: pyridine, quinoline, and phen. In the case of ligand **2**, the phen is replaced by bpy; for ligand **3**, the pyridine and quinoline are linked by a dimethylene bridge. These structural variations influence both the rigidity of the system and the planarity. Assuming that the heteroaromatic


DOI: 10.1021/acs.inorgchem.5b00915
Inorg. Chem. 2015, 54, 7873−7884

rings are essentially planar, flexibility is thus derived from the σ-bonds that separate these subunits. For ligand **2**, where bpy replaces phen, there are 3 σ-bonds and the corresponding Co complex is the least planar. The resulting nonplanarity of **2** in the complex results mainly from the N3 pyridine ring rotating out of the mean plane, creating a C10−C14−C15−N3 dihedral angle of 40.92° and a N3−C19−C20−N4 dihedral angle of 17.26°. By comparison, the corresponding dihedral angles for $[Co(\mathbf{3})(OH_2)Cl]^+$ are 25.45° (C12−C16−C17−N3) and 2.24° (N3−C21−C25−N4), respectively. It is interesting that the dimethylene bridge in $[Co(\mathbf{3})(OH_2)Cl]^+$ provides a N1−C5−C9−N2 dihedral angle of 12.19° which is quite similar to the unbridged complex $[Co(\mathbf{2})Cl_2]$ at 12.88°. In the former case, the distortion is caused by the relief of eclipsing C−H interactions in the bridge, whereas, in the latter, the twisting avoids interaction between C4−H and C7−H.

The electronic absorption spectra of the four cobalt complexes were measured in dry DMF, and the results are given in Table S3 in the Supporting Information and illustrated by Figure 2. The longest wavelength band for each complex is

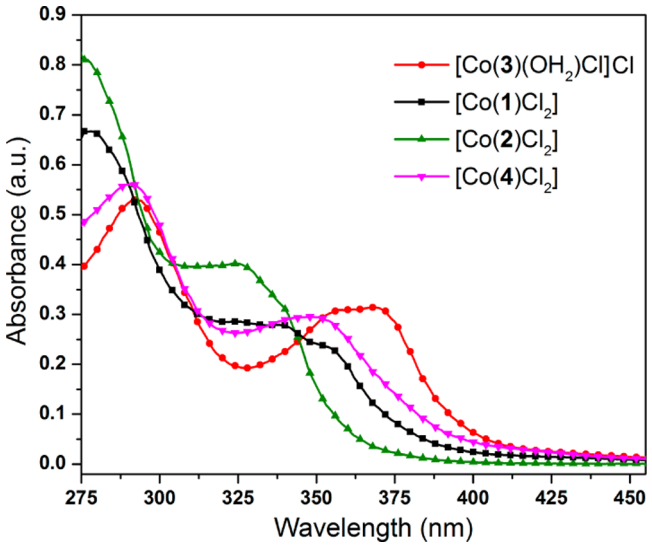


**Figure 2.** UV-vis absorbance of Co complexes (20 μM in DMF).

associated with a metal-to-ligand charge transfer (MLCT) involving the promotion of an electron from a metal-based d-orbital to a ligand-based π*-orbital. The more rigid and planar the ligand, the better the π-delocalization in the excited state and, thus, the lower in energy the π* level, as well as the energy of the MLCT transition. For the series of four Co complexes, the one involving ligand **3** shows the longest wavelength absorption, implying the most delocalized π-system. The $\lambda_{max}$ for $[Co(\mathbf{2})Cl_2]$ occurs at the shortest wavelength reflecting the flexibility associated with three σ-bonds in the tetradentate framework. The electronic spectra of $[Co(\mathbf{1})Cl_2]$ and $[Co(\mathbf{1})Br_2]$ in DMF (Figure S17 in the Supporting Information) have similar profiles, since halogen anions are weak-field ligands and have a similar effect on the cobalt center. The absorption spectra of $[Co(\mathbf{1})Cl_2]$ and $[Co(\mathbf{1})Br_2]$ in $H_2O$ are almost identical, implying halogen/$OH_2$ exchange after dissolution of both complexes in water, which was also supported by the electrochemical studies discussed below.

The four Co(II) complexes are all soluble in water at a concentration of 1 mM. In our earlier study, we found that the UV-vis absorption of $[Co(\mathbf{1})Cl_2]$ changed as the pH was varied from 8.6 to 11.2.[37] Considering the extraordinarily long Co(II)−Cl bond of this complex, we suggested that one or both chloride ligands may dissociate after the complex is dissolved in water. The pH-dependent absorption change was associated with deprotonation of a Co(II)-aqua species derived from $[Co(\mathbf{1})Cl_2]$. In this report, we studied the relative Gibbs free energies of all charged cobalt-containing species that are likely present in the water solution of $[Co(\mathbf{1})Cl_2]$ with DFT at the M06-L/LACV3P**++ level of theory (see Scheme S1 and Figure S18 in the Supporting Information). All simulated Co(II) species prefer a low-spin ($S$ = 1/2) configuration. The four Co(II)-ppq species displayed in Scheme 2 are estimated to be more stable in water than $[Co(\mathbf{1})Cl_2]$, by ∼3−5 kcal/mol. The $[Co(\mathbf{1})(OH_2)_2]^{2+}$ and $[Co(\mathbf{1})(OH_2)Cl]^+$ exhibit the lowest relative energy among these Co(II) species and thus are regarded as dominant in the aqueous solution. The free-energy change of the conversion from $[Co(\mathbf{1})(OH_2)Cl]^+$ to $[Co(\mathbf{1})(OH_2)_2]^{2+}$ is almost zero, indicating almost-equal concentrations. Equilibrium constants between these Co(II) species were derived from their calculated free-energy differences (see Scheme 2). The simulated Co(II)−O(aqua) bond lengths are 2.14−2.20 Å, close to the Co1−O1W length (2.195 Å) in $[Co(\mathbf{3})(OH_2)Cl]^+$. The Co(II)-aqua coordination bonds might be favored by hydrogen bonding between the aqua ligand and solvent water molecules. Similar aqua/$Cl^-$ ligand exchange is expected to occur for the other Co(II) catalysts of the series, because they all exhibit a long Co(II)−Cl bond and show substantial solubility in water. The Co−N(**1**) bond distances in the optimized structure of $[Co(\mathbf{1})(OH_2)_2]^{2+}$ are very close to the Co−N(**1**) bonds in the solid structure of $[Co(\mathbf{1})Cl_2]$.[37] Substitution of chloride by aqua does not seem to affect the equatorial ligand coordination with Co(II).

**Light-Driven Hydrogen Evolution.** The photocatalytic $H_2$-evolving activity of these cobalt complexes was evaluated under homogeneous aqueous conditions using $[Ru(bpy)_3]^{2+}$ as the photosensitizer (PS), ascorbic acid ($H_2A$) as a sacrificial electron donor, and a blue LED ($\lambda_{max}$ = 469 nm) as the light source. The rate of $H_2$ evolution was monitored in real time using a pressure transducer and the percentage of generated hydrogen in the headspace was calibrated by GC at the end-point of each trial. All four catalysts drive photocatalytic proton reduction under moderately acidic conditions (pH 3.5−5.5) and they all show their fastest $H_2$-evolving rate at pH 4.5 (see

**Scheme 2. Equilibrium of Cobalt-Containing Species in the Water Solution of $[Co(1)Cl_2]$**[a]

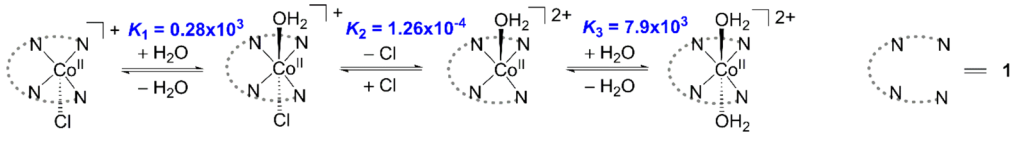


[a]The equilibrium constants are derived from DFT calculated energy differences.



DOI: 10.1021/acs.inorgchem.5b00915
Inorg. Chem. 2015, 54, 7873−7884

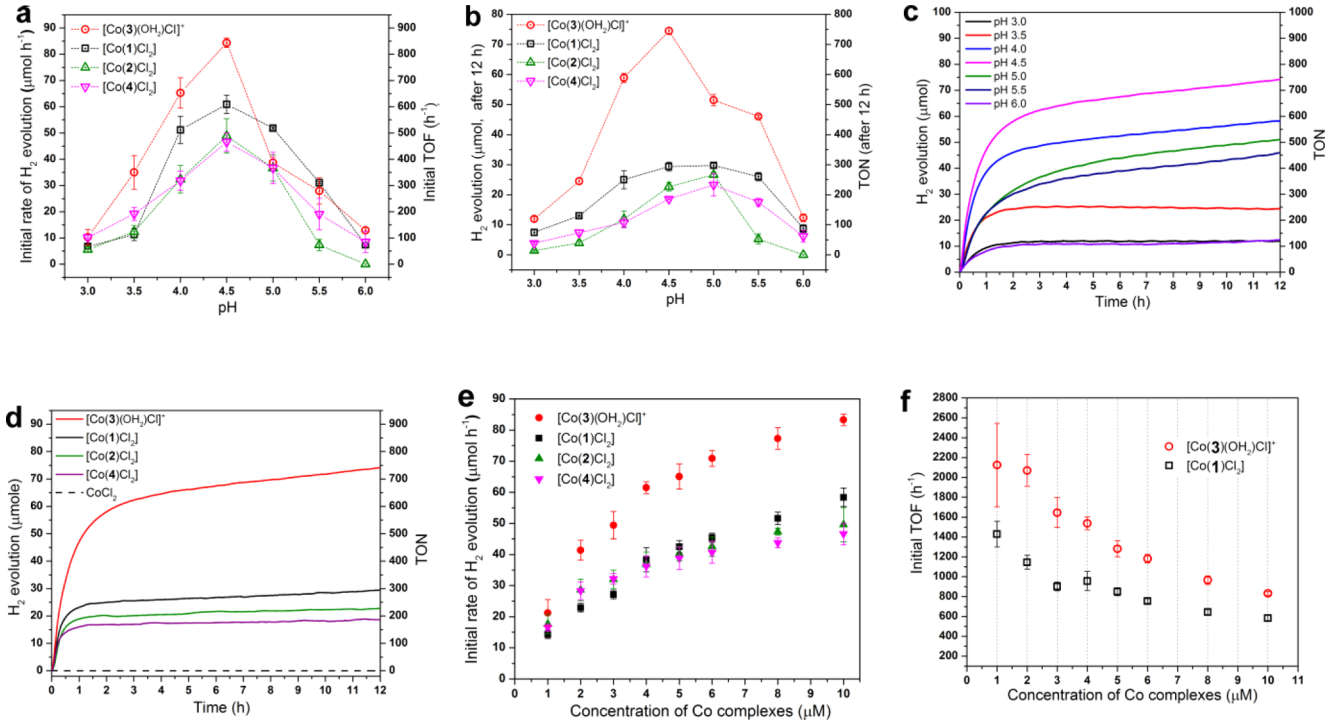


**Figure 3.** (a) Initial rate and (b) $H_2$ production (after 12 h) of photocatalytic hydrogen evolution by Co complexes at various pH values. Photocatalytic hydrogen evolution versus time plots (c) by $[Co(\mathbf{3})(OH_2)Cl]^+$ at various pH values and (d) by different Co complexes at pH 4.5. (e) Initial rate and (f) initial TOF of photocatalytic hydrogen evolution by Co complexes at various concentrations of the catalyst. Conditions: for panels a–d, 10 $\mu$M catalyst and 0.4 mM $[Ru(bpy)_3]Cl_2$ in 10 mL 0.3 M L-ascorbic acid solution (pH adjusted by addition of NaOH); for panels e and f, 0.4 mM $[Ru(bpy)_3]Cl_2$ in 10 mL 0.3 M ascorbic acid solution (pH 4.5). Initial rate of $H_2$ production was calculated by linearly fitting the $H_2$ evolution vs time plot for the first 15 min. Initial TOF = (initial rate of $H_2$ production)/(concentration of catalyst).

Figure 3a). Under these optimized conditions, an initial TOF (turnover frequency) of 848 $h^{-1}$, according to the catalyst (10 $\mu$M), was achieved by $[Co(\mathbf{3})(OH_2)Cl]^+$, which is considerably greater than that by $[Co(\mathbf{1})Cl_2]$ (610 $h^{-1}$), $[Co(\mathbf{2})Cl_2]$ (490 $h^{-1}$) or $[Co(\mathbf{4})Cl_2]$ (466 $h^{-1}$). Meanwhile, the highest TON of 745 (per catalyst) was also observed in the composite system with $[Co(\mathbf{3})(OH_2)Cl]^+$ as a PRC after 12 h reaction (Figure 3d). For the same period of time, $[Co(\mathbf{1})Cl_2]$, $[Co(\mathbf{2})Cl_2]$, and $[Co(\mathbf{4})Cl_2]$ only afford TON = 200–300. Therefore, ligand **3** affords not only the fastest but also the most robust cobalt PRC, compared with other ligands in the family. The superior performance of $[Co(\mathbf{3})(OH_2)Cl]^+$ is clearly evidenced by the comparison shown in Figures 3d and 3f. In a control experiment, no photocatalytic $H_2$ generation was observed when $CoCl_2$ was employed in place of the catalysts derived from **1**–**4** (Figure 3d, dashed line).

The rates of visible light-driven $H_2$ evolution were also measured at catalyst concentrations of 1–10 $\mu$M (Figure 3e), while the concentrations of other system components were kept constant. The $H_2$-evolving rates rise as the catalyst concentration increases. However, the rates do not scale up linearly, depending upon the concentration of the catalyst. Accordingly, the initial TOF declines as the catalyst concentration is increased (Figure 3f). This decline is probably due to less effective intermolecular electron transfer and more severe catalyst aggregation at higher concentrations. The efficiency of $[Co(\mathbf{3})(OH_2)Cl]^+$ is superior to the other catalysts at every concentration tested. At a catalyst concentration of 1 $\mu$M, an initial TOF of 2125 $h^{-1}$ (per catalyst) was achieved by $[Co(\mathbf{3})(OH_2)Cl]^+$, compared to 1430 $h^{-1}$ by $[Co(\mathbf{1})Cl_2]$. At a catalyst concentration of 10 $\mu$M, the initial TOF of $[Co(\mathbf{3})(OH_2)Cl]^+$ and $[Co(\mathbf{1})Cl_2]$ decrease to 848 $h^{-1}$ and 610 $h^{-1}$, respectively. If the concentration of $[Ru(bpy)_3]^{2+}$ was varied from 0.02 mM to 0.1 mM, using $[Co(\mathbf{3})(OH_2)Cl]^+$ as the catalyst (5 $\mu$M), a linear dependence of $H_2$ evolution on the concentration of sensitizer was observed (Figure S19 in the Supporting Information). When the concentration of $[Ru(bpy)_3]^{2+}$ exceeds 0.1 mM (30 equiv), the rate versus concentration plot deviated from the linear relationship and begins to level off.

In the experiments described above, the concentration of $[Ru(bpy)_3]^{2+}$ is usually ~40-fold greater than the concentration of catalyst, whereas $H_2A$ is in large excess, typically more than 100-fold the concentration of $[Ru(bpy)_3]^{2+}$. The thermodynamics and kinetics of electron transfer processes in such a three-component system ($H_2A$-$[Ru(bpy)_3]^{2+}$-catalyst) have been well-established. The system is prone to undergo a reductive quenching pathway upon irradiation.[20,31,40] The excited state of $[Ru(bpy)_3]^{2+}$ has a reduction potential of +0.84 V vs NHE and thus it can be reductively quenched by $H_2A/HA^-$ (oxidation potential of approximately +0.17 V vs NHE). Each $H_2A$ molecule provides two electrons and two protons, resulting in hydrated dehydroascorbic acid as the dominant oxidation product.[41] The rate constant of electron transfer from $H_2A$ to $[Ru(bpy)_3]^{2+*}$ was estimated to be $2.6 \times 10^7$ $M^{-1}$ $s^{-1}$ at pH 4.0.[19,20] The oxidation potential of $[Ru(bpy)_3]^+$ (−1.26 V vs NHE) is thermodynamically negative enough to reduce the Co(II) catalyst to a crucial state that triggers catalytic $H_2$ evolution occurring in a pH 4.5 buffer. The net reaction of $H_2$ evolution can be expressed as $H_2A \rightarrow H_2 + A$, which is thermodynamically unfavorable by 0.41 V at pH ≥4.[40] Therefore, the overall light-driven $H_2$ production


DOI: 10.1021/acs.inorgchem.5b00915
Inorg. Chem. 2015, 54, 7873–7884

represents direct conversion from solar energy to chemical energy in the form of the H−H bond. It is noteworthy that the emission of $[Ru(bpy)_3]^{2+}$ does not bleach in the presence of the Co(II) catalysts at the concentrations employed in the photocatalytic experiments (Figure S20 in the Supporting Information). This observation confirms that oxidative quenching of the excited sensitizer by the catalyst is not involved in the light-driven $H_2$ evolution reaction.

**Electrochemical Behavior.** The complexes $[Co(\mathbf{2})Cl_2]$, $[Co(\mathbf{3})(OH_2)Cl]^+$, and $[Co(\mathbf{4})Cl_2]$ were evaluated by cyclic voltammetry (CV) in DMF (Figure S22 in the Supporting Information). All three complexes show CV profiles very similar to that of $[Co(\mathbf{1})Cl_2]$: one oxidation event in the anodic sweep assigned to a Co(II/III) process and three discrete reduction events in the cathodic sweep assigned to a formal Co(II) → Co(I) → Co(0) → Co(−I) redox sequence.[37] The Co(II/III) potentials for the series of Co(II) complexes fall in the narrow range of −0.17 to −0.26 V (vs ferrocene, Table 2).

**Table 2. Selected Redox Potentials of Co Complexes**[a]

| complex | DMF (V vs $Cp_2Fe^{+/0}$) | pH 4.5 phosphate buffer (V vs NHE)[b] |
|---|---|---|
| $[Co(\mathbf{1})Cl_2]$ | −0.26, −1.22[r], −1.47[r], −1.82[r] | 0.74[r], −0.48[r], −0.60[c], −0.95[d] |
| $[Co(\mathbf{2})Cl_2]$ | −0.20[r], −1.09[r], −1.48[r], −1.76[r] | 0.72[r], −0.51[r], −0.72[c], −0.91[d] |
| $[Co(\mathbf{3})(OH_2)Cl]^+$ | −0.23[r], −1.02[r], −1.50[r], −1.76[r] | 0.75[r], −0.49[r], −0.61[c], −0.92[d] |
| $[Co(\mathbf{4})Cl_2]$ | −0.17[r], −1.29[r], −1.60[r], −1.84 | 0.83[r], −0.59[r], −0.68[c], −0.94[d] |

[a]Values with a superscripteed "r" denote values obtained with reversible CV waves. [b]Referenced to $E^{3+/2+}$ of $[Ru(bpy)_3]^{2+}$ (1.26 V vs NHE). [c]Deposition occurs. [d]Potential at a current density of 10 mA/cm$^2$.

The three reduction potentials are also quite similar for the four Co(II) complexes. Apparently, structural differences among ligands **1**−**4** does not affect their redox properties substantially. CVs of this series of Co(II) complexes were also conducted in pH 4.5 aqueous buffer (Figures S21 and S22 in the Supporting Information), which is the optimal pH for photocatalytic $H_2$ evolution by these catalysts. Negatively charged cobalt-aqua species are dominant in the aqueous medium and they showed different redox profiles, compared to the CVs performed in DMF. In addition, square wave voltammograms were measured to more precisely determine the redox potentials (Figure S22 in the Supporting Information).

Besides a Co(II/III) wave at ∼0.75 V vs NHE (Figure S23 in the Supporting Information), all the CVs performed in pH 4.5 phosphate buffer reveal a reversible redox wave at approximately −0.50 V and an irregular redox wave at approximately −0.68 V vs NHE (Table 2). The reversibility of the first redox wave was verified by examination of $[Co(\mathbf{3})(OH_2)Cl]^+$, whose current peak of the wave is proportional to both the square root of the scan rate (Figure S24 in the Supporting Information) and the concentration of the complex (Figure S25 in the Supporting Information). These observations determine the redox event to be a diffusion-controlled process. Considering that chloride/$H_2O$ exchange occurs under aqueous conditions, the first reduction waves were designated as $[Co(II)\text{-aqua}]^{2+}$/$[Co(I)\text{-aqua}]^+$ processes. The irregular reduction waves at more negative potential correspond to the reduction of $[Co(I)\text{-aqua}]^+$ to $[Co(0)\text{-aqua}]$ species leading to the deposition of the neutral $[Co(0)\text{-aqua}]$ species on the surface of the electrode during the cathodic sweep and a stripping process during the anodic sweep. The observation of a deposition/stripping process is consistent with the fact that a neutral $[Co(0)\text{-aqua}]$ species is not as soluble in water as a charged cobalt species such as $[Co(I)\text{-aqua}]^+$. Similar phenomena were also observed for other water-soluble molecular PRCs.[42] A catalytic current for proton reduction was observed for all Co(II) complexes with the current onset at approximately −0.85 V vs NHE.

Since $[Co(\mathbf{3})(OH_2)Cl]^+$ attained the highest TOF in the light-driven $H_2$ evolving experiments, its electrochemical behavior was investigated in a series of phosphate buffers with pH = 3.5−6.5, which is also the pH range applied in the light-driven $H_2$ evolution experiments. As illustrated by the square wave voltammograms at various pH (Figure 4, left), the $[Co(II)\text{-aqua}]^{2+}/[Co(I)\text{-aqua}]^+$ potential of $[Co(\mathbf{3})(OH_2)Cl]^+$ is independent of the pH and thus excludes proton coupled electron transfer. The wave of the succeeding reduction of $[Co(I)\text{-aqua}]^+$ moves slightly more negative as the pH increases (Figure 4, center). Moreover, the potential of the catalytic current, for example, at a density of 20 mA/cm$^2$, is reduced as the pH decreases indicating the involvement of a coupled proton transfer. The electrochemical behavior of $[Co(\mathbf{3})(OH_2)Cl]^+$ upon varying pH was similar to what we reported for $[Co(\mathbf{1})Cl_2]$ in a previous study.[37] The deposition

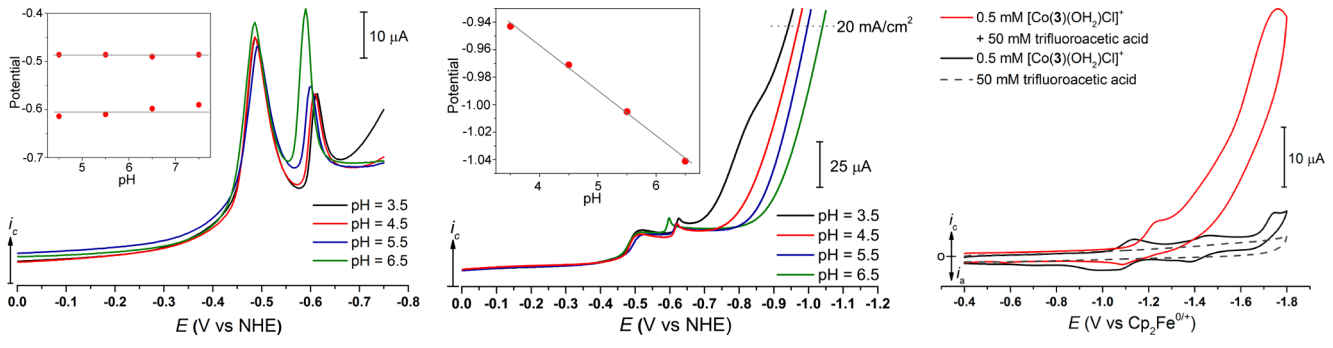


**Figure 4.** (Left) Square wave voltammograms of $[Co(\mathbf{3})(OH_2)Cl]^+$ (1.0 mM) in phosphate buffer (0.1 M) at various pH; inset shows potentials of redox waves at different pH (amplitude = 25 mV, step potential = 4 mV, and frequency = 15 Hz. (Center) Cathodic scan of cyclic voltammograms of $[Co(\mathbf{3})(OH_2)Cl]^+$ (1.0 mM) in phosphate buffer (0.1 M) at various pH,; inset shows potentials of catalytic current (20 mA/cm$^2$) at different pH, scan rate = 100 mV/s. (Right) Cyclic voltammograms of $[Co(\mathbf{3})(OH_2)Cl]^+$ (0.5 mM) in $H_2O$/DMF mixture (v/v = 20/80, 0.1 M $(^nBu_4N)PF_6$) in the presence or absence of trifluoroacetic acid (50 mM), scan rate = 50 mV/s.



DOI: 10.1021/acs.inorgchem.5b00915
Inorg. Chem. 2015, 54, 7873−7884

**Scheme 3. Proposed Redox Sequence of $[Co(1)(OH_2)_2]^{2+}$ in Aqueous Buffer Solution**

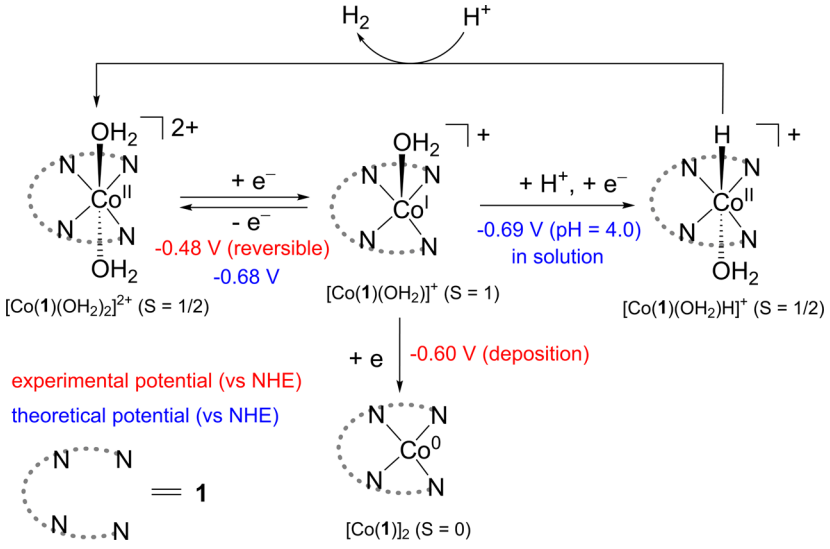


of reduced cobalt complexes that is inevitable in aqueous buffer medium, however, may interfere with the profile of the catalytic current. Therefore, CVs of $[Co(\mathbf{1})Cl_2]$ and $[Co(\mathbf{3})(OH_2)Cl]^+$ were also investigated in $H_2O$/DMF (20/80 by volume) mixture, which is able to avoid deposition of the Co(0) species and yet provide enough solvation for dissociation of the chloride ligands. In this medium, both complexes display two reversible one-electron redox waves at about −1.10 and −1.45 V vs ferrocene (+/0) corresponding to the Co(II)/Co(I) and Co(I)/Co(0) processes, respectively (Figure S29 in the Supporting Information). In the presence of 50 mM trifluoroacetic acid, a salient cathodic current emerged in the CV of $[Co(\mathbf{3})(OH_2)Cl]^+$ when scanning beyond the Co(II)/Co(I) redox potential (Figure 4, right). Such a current enhancement was also observed in the CV of $[Co(\mathbf{1})Cl_2]$ (Figure S30 in the Supporting Information). These significant current enhancements indicate catalytic proton reduction by a molecular cobalt complex.

The CV of $[Co(\mathbf{1})Br_2]$ in DMF (Figure S26 in the Supporting Information) shows consecutive irreversible redox waves that are completely different from the redox waves in the CV of $[Co(\mathbf{1})Cl_2]$. This difference is probably due to dissociation of bromide when $[Co(\mathbf{1})Br_2]$ is reduced in DMF. In aqueous buffer, however, the CVs of $[Co(\mathbf{1})Cl_2]$ and $[Co(\mathbf{1})Br_2]$ are almost identical (Figures S27 and S28 in the Supporting Information). Redox events in their CVs occur at the same potentials reflecting a uniform cobalt species in aqueous solution. This finding further substantiates our suggestion that the halogen ligands are replaced by water after dissolution of these complexes in water, where $[Co(II)\text{-aqua}]^{2+}$ complexes become the dominant species.

## DISCUSSION

Despite different catalytic activities, this family of Co(II) complexes all show similar electrochemical behavior in either organic or aqueous solution. Their well-resolved reversible CV waves in DMF indicate that these Co(II) complexes remain intact at Co(III), Co(I), and Co(0) oxidation states. The replacement of chloride ligands by DMF does not occur. Voltammetry was not conducted in other organic solvents, because of insufficient solubility of these cobalt complexes. The electrochemical properties of these complexes in aqueous solution are more meaningful, because their properties are directly related to the catalytic path for light-driven $H_2$ evolution that is carried out in aqueous buffer. However, the deposition of neutral Co(0) species makes the determination of certain redox process less certain. In order to help elucidate key intermediates that might be involved in the catalytic cycle of light-driven proton reduction, the redox sequence of $[Co(\mathbf{1})Cl_2]$ in aqueous buffer was investigated using a DFT theoretical model as a prototype for the whole series of catalysts. A water molecule was employed as a hydrogen bond acceptor for each polar hydrogen (aqua group) when the geometry of the cobalt species was simulated.

As described above, the species $[Co(\mathbf{1})(OH_2)_2]^{2+}$ and $[Co(\mathbf{1})(OH_2)Cl]^+$ predominate in an aqueous solution of $[Co(\mathbf{1})Cl_2]$. Reduction of $[Co(\mathbf{1})(OH_2)_2]^{2+}$ or $[Co(\mathbf{1})(OH_2)Cl]^+$ leads to the formation of a formal Co(I) species. We searched plausible configurations of this Co(I) intermediate and found that it prefers a high-spin ($S$ = 1) pyramidal geometry with one aqua ligand (see Scheme 3 and Figure S31 in the Supporting Information). Compared to the optimized structure of $[Co(\mathbf{1})(OH_2)_2]^{2+}$, the Co−O(aqua) bond (2.068 Å) in the simulated structure of $[Co(\mathbf{1})(OH_2)]^+$ is shorter by 0.08−0.14 Å, whereas the average of Co−N(**1**) bond distances are longer, by ∼0.1 Å. Accordingly, the phen−quinoline torsion angle of **1** increases after this reduction event while the quinoline−pyridine torsion angle decreases. The calculated redox potential for this $[Co(\mathbf{1})(OH_2)_2]^{2+}/[Co(\mathbf{1})(OH_2)]^+$ step is −0.68 V (vs NHE) that is close to the potential observed in aqueous buffer.

The one-electron reduction of $[Co(\mathbf{1})(OH_2)]^+$ yields a formally neutral Co(0) species which deposits on the surface of the working electrode, as observed in CV waves of $[Co(\mathbf{1})Cl_2]$ in aqueous buffer. Such a phase transfer process is much less unlikely to happen in a photocatalytic system, because of the low concentration of the cobalt complex. Therefore, different scenarios are considered in the theoretical model to address corresponding circumstances. If a well-organized neutral $[Co(\mathbf{1})]_2$ dimer was employed to mimic the deposited substrate, consisting of two stacked $[Co(\mathbf{1})]$ monomers with a Co−Co distance of 3.008 Å and an overall closed-shell (Figure S32 in the Supporting Information), the $[Co(\mathbf{1})(OH_2)]^+/[Co(\mathbf{1})]_2$ redox event is calculated to occur at a more


DOI: 10.1021/acs.inorgchem.5b00915
Inorg. Chem. 2015, 54, 7873−7884

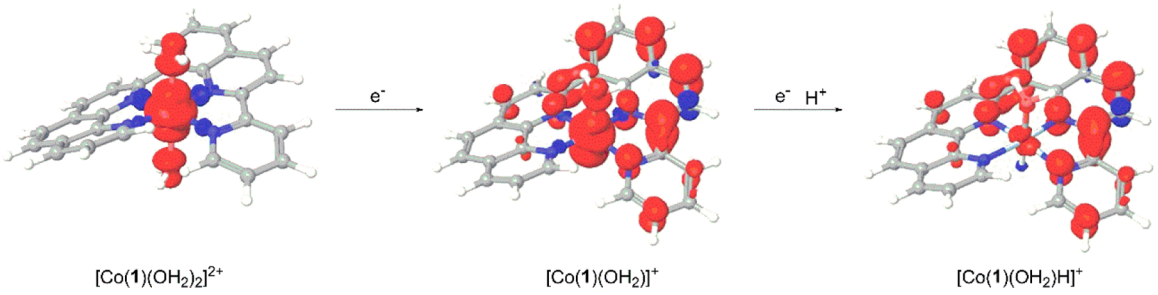


**Figure 5.** Spin density plots of the open-shell cobalt species. [Color code: dark red corresponds to $\alpha$ spin; dark blue corresponds to $\beta$ spin.] Solvated water molecules are not shown.

positive potential (−0.35 V vs NHE) than that (−0.60 V) observed in CV.[43] Simulation of the deposition by dimerization, however, may overestimate the effect of phase transfer. If a neutral monomer $[Co(\mathbf{1})(OH_2)]$ is assumed to be generated and present either in the homogeneous phase or on the electrode surface, the reduction potential from $[Co(\mathbf{1})(OH_2)]^+$ to $[Co(\mathbf{1})(OH_2)]$ was calculated to be −0.92 V, which is more negative than the measured potential of −0.60 V. The two scenarios illustrate how a congregation of the formal Co(0) reduction product can influence the redox potential. The difference between experimental and theoretical potentials for the deposition process derives from complexity of the deposited Co(0) species that is neither as well-organized as a dimer nor as simple as a monomer.

Alternatively, monomer Co(I) intermediate $[Co(\mathbf{1})(OH_2)]^+$ can undergo a PCET process and form a formal Co(II) hydride intermediate which, according to our theoretical model, favors a low-spin ($S$ = 1/2) octahedral configuration denoted as $[Co(\mathbf{1})(OH_2)H]^+$ (Figure S33 in the Supporting Information). The p$K_a$ of hydride species was calculated to be 6.9. Therefore, the $[Co(\mathbf{1})(OH_2)]^+/[Co(\mathbf{1})(OH_2)H]^+$ PCET process is thermodynamically favored in homogeneous environment when the pH of the medium is <6.9. The calculated potential of the $[Co(\mathbf{1})(OH_2)]^+/[Co(\mathbf{1})(OH_2)H]^+$ redox is −0.69 V vs NHE at pH 4.0. The thermodynamic relationships of cobalt species in aqueous medium is concluded in Scheme S2 in the Supporting Information. However, this PCET process is rarely observed in CVs of $[Co(\mathbf{1})Cl_2]$ performed in an aqueous buffer, because deposition of Co(0) species on the electrode surface is predominant in the competition.

The CV of $[Co(\mathbf{1})Cl_2]$ in $H_2O$/DMF (20/80 by volume) does not involve deposition of a cobalt species. In the presence of acid, significant catalytic current was initiated at a more negative potential than the Co(II)/(I) redox potential and thus should be triggered by further reduction of the Co(I) species (Figure S30 in the Supporting Information). On the basis of the combined experimental and theoretical results, we propose a scheme for the catalytic cycle of proton reduction by the complex $[Co(\mathbf{1})Cl_2]^+$ (see Scheme 3) in a homogeneous system. The hydride intermediate $[Co(\mathbf{1})(OH_2)H]^+$ triggers the H−H bond formation of a fast rate. On the electrode surface, however, the complex is reduced to a Co(0) species, which deposits on the electrode first and is probably protonated at a slow rate during cathodic scan afterward, forming the active hydride intermediate. Involvement of the protonation was corroborated by the negative shift of the onset of the catalytic current dependent on the pH increase in the CV experiments.[37] A broad redox wave extrudes from the catalytic current curve at 0.85 V under pH 3.0 conditions.[37] This wave might indicate the formation of hydride $[Co(\mathbf{1})(OH_2)H]^+$ redox via PCET or protonation. Similarly, the catalytic onset for $[Co(\mathbf{3})(OH_2)Cl]^+$ experiences a negative shift as the pH increases (Figure 4, middle). Because of the similar electrochemical performance of $[Co(\mathbf{1})Cl_2]$ and other complexes in the series, in both aqueous buffer and $H_2O$/DMF mixture, the catalytic pathway proposed for $[Co(\mathbf{1})Cl_2]$ (Scheme 3) can also be applied to the other catalysts discussed in this paper.

The spin density of open shell cobalt intermediates was calculated and is shown in Figure 5 for the redox sequence of $[Co(\mathbf{1})(OH_2)_2]^{2+} \rightarrow [Co(\mathbf{1})(OH_2)]^+ \rightarrow [Co(\mathbf{1})(OH_2)H]^+$. The spin density represents the net electron density of unpaired electrons for the cobalt species and provides an intuitive method to track where the electron ends up during reduction, to demonstrate the contribution of the cobalt center and the ligand in the redox steps. The first reduction process is entirely ligand-based and the spin density of $[Co(\mathbf{1})(OH_2)]^+$ locates mainly on the quinoline and pyridine part of the ligand. The unpaired electron at the metal center remains in an orbital, which is mainly the $3dz^2$ orbital on cobalt with some interaction with the $sp^3$ orbital on the aqua ligand. The consecutive reduction step is, however, metal-based. The electron appears to go to the $3dz^2$ orbital, which is protonated to form the hydride. The spin density of $[Co(\mathbf{1})(OH_2)H]^+$ is distributed principally over the quinoline and pyridine moieties but not the phenanthroline moiety of ligand **1**. This distribution may be associated with two features. First, torsion between phenanthroline and quinoline impedes spin density distribution over the entire ligand. Second, greater conjugation of quinoline with the pyridine rather than the phenanthroline moiety makes the former a better electron acceptor. Since the first reduction is ligand-based, $[Co(\mathbf{1})(OH_2)]^+$ is better described as $[Co^{II}(\mathbf{1}^{-\bullet})(OH_2)]^+$. In the second reduction, the unpaired electron remains on the ligand, indicating that the $[Co(\mathbf{1})(OH_2)H]^+$ should formally be described as $[Co^{III}(\mathbf{1}^{-\bullet})(OH_2)H]^+$. The noninnocent role of ligand **1** facilitates the reduction to $[Co^{III}(\mathbf{1}^{-\bullet})(OH_2)H]^+$ by avoiding the formally metal-centered Co(I)/Co(0) redox step which demands a much more negative potential.

The replacement of the phen moiety by bpy in ligand **2** does not influence the reduction steps leading to Co hydride formation, because the phen moiety has very little spin density in the resulting Co hydride species, as described above. Nor does the linking of the 2-(pyrid-2′-yl)quinoline subunit by a dimethylene or trimethylene bridge in **3** or **4** benefit the [Co(I)-aqua]$^+$/[Co(II)−H]$^+$ reduction, because the quinoline−pyridine moiety in $[Co(\mathbf{1})(OH_2)H]^+$ is already quite planar and thus the bridging cannot further enhance its conjugation. Therefore, the spin density analysis based on


DOI: 10.1021/acs.inorgchem.5b00915
*Inorg. Chem.* 2015, 54, 7873−7884

complex $[Co(\mathbf{1})(OH_2)_2]^{2+}$ suggests the generation of an active $[Co(II)-H]^+$ species at similar potentials for catalysts with ligands **1**–**4**.

It is possible that the torsion between phen and quinoline subunits in $[Co(\mathbf{1})(OH_2)H]^+$ could be relieved if the pyridine subunit dissociates from the cobalt center. In this case, the spin density is more likely to distribute over the now more planar phen–quinoline moiety. Compared to the spin density of $[Co(\mathbf{1})(OH_2)H]^+$ in Figure 5, the redistribution of spin density through reorganization of coordination geometry may lead to a more stable state of the $[Co(II)-H]^+$ species, because the phen–quinoline subunit is more delocalized than the corresponding quinoline–pyridine subunit. However, the $[Co(II)-H]^+$ intermediate could lose its catalytic activity after dissociation of the pyridine subunit. Thus, the dimethylene bridge in ligand **3** may improve the lifetime and higher TON of $[Co(\mathbf{3})(OH_2)Cl]^+$, compared with the other catalysts in the series by hindering the dissociation of pyridine.

Note that the phen–quinoline torsion angle (N19–C18–C23–C30) (Figure S27 in the Supporting Information) for the $[Co(\mathbf{1})(OH_2)]^+$ state (30.6°) is much greater than that for the $[Co(\mathbf{1})(OH_2)H]^+$ state (15.4°) (Figure S33 in the Supporting Information). Thus, the complex reorganizes itself by flattening the ligand through the $[Co(\mathbf{1})(OH_2)]^+/[Co(\mathbf{1})(OH_2)H]^+$ PCET step. Similar reorganization may also occur at the subsequent key H–H bond formation step. More planarity of the ligand can help to reduce the energy barrier of such geometric reorganization.[44] This feature may help to explain the relatively higher TOF of photocatalytic $H_2$ evolution by the Co catalyst containing ligand **3**, rather than **1**, **2**, or **4**.

## CONCLUSION

A series of tetradentate polypyridine ligands (**2**–**4**) were prepared and characterized as analogues of the previously reported ppq ligand (**1**). They readily coordinate with Co(II) and form octahedral Co complexes bearing axial chloride or aqua ligands. After being dissolved in aqueous solution, these complexes are prone to dissociate an axial chloride ligand and associate with an aqua ligand. All complexes are capable of catalyzing light-driven $H_2$ evolution in homogeneous aqueous medium with TOF up to 2125 $h^{-1}$ per catalyst. Combined experimental and theoretical evidence suggests a catalytic pathway involving formally Co(I)-aqua and Co(II)-H intermediates. These tetradentate ligands are not innocent in the Co(II)-aqua to Co(I)-H reduction and, thus, the formally Co(II) to Co(I) aqua and following to Co(II) hydride steps avoid metal-centered redox processes, which usually require more negative reduction potentials. The enhanced rigidity of ligand **3**, relative to its analogues, increases the efficiency of catalyst $[Co(\mathbf{3})(OH_2)Cl]^+$ by lowering the energy barrier for reorganization on one hand, and improving its robustness by inhibiting potential dissociation of the pyridine moiety on the other. These findings indicate how catalytic activity is influenced by rigidity and conjugation of the polypyridine ligand platform, in conjunction with electronic effects. This study helps us to understand the correlation between coordination environment and the catalytic activity of mononuclear Co PRCs, which might inspire the design and synthesis of more efficient and durable catalysts. Future work will focus on the modification of Co-ppq catalyst with electron-withdrawing substitutes in order to reduce the catalytic overpotential. Meanwhile, we are also considering the installation of bulky groups on the ligand to alleviate congregation of these Co catalysts.

## EXPERIMENTAL SECTION

**Materials and Methods.** The 8-bromo-2-(pyrid-2′-yl)quinoline (**5**),[37] 2-amino-3-bromobenzaldehyde (**7**),[45] 8-amino-7-quinolinecarbaldehyde,[46] 6,7-dihydroquinolin-8(5H)-one (**8a**),[46] and cyclohepta[*b*]pyridin-9-one (**8b**)[47] were prepared by following a published method. The synthesis of **1** (ppq) and $[Co(\mathbf{1})Cl_2]$ has been reported previously.[37] All other reagents and solvents are commercially available and were used as received, unless otherwise noted. Mass spectra were measured on Thermo LCQ deca XP ESI-MS. Elemental analyses were performed by NuMega Resonance Laboratories (San Diego, CA). Electronic absorption spectra were recorded with a Varian Cary-50 Bio spectrophotometer and were corrected for the background spectrum of the solvent. Electrochemical measurements were carried on a BAS Epsilon potentiostat at 20 °C using a glassy carbon disk (diameter = 3 mm) as the working electrode, a platinum wire as the counter electrode, and a saturated calomel electrode (SCE) as the reference electrode. The working electrode was polished by alumina (0.05 μm) before every measurement. The employed electrolyte is either a series of phosphate buffers (0.1 M) or DMF solution of $(^nBu_4N)PF_6$ (0.1 M). Potentials were converted to versus NHE by using $[Ru(bpy)_3]^{2+}$ ($E^{3+/2+}$ = 1.26 V vs NHE)[48] as an internal reference in aqueous buffers. Ferrocene ($Cp_2Fe^{+/0}$)[49] was used as an internal references in the DMF-based electrolyte. The pH value of the phosphate buffer was measured with a Thermo Scientific Orion Star A211 pH Benchtop Meter. Before any electrochemical sweep measurement was carried out, the sample solution was degassed thoroughly with argon.

**Light-Driven Hydrogen Evolution.** Hydrogen evolution was measured using a custom-built 25 mL round-bottom flask (Figure S34) connected to a pressure transducer (Omega PXM409–002 BAUSBH, pressure range 0–2 bar) via a Teflon spacer. In a typical run, the custom-built flask was charged with 10 mL of ascorbic acid water solution (0.3 mM, titrated to a certain pH with NaOH) containing various amounts of $[Ru(bpy)_3]Cl_2$ and cobalt catalysts, together with a stirring bar. The flask was degassed by bubbling with Ar through a threaded glass neck on the flask for 15 min and then sealed with a septum. The absence of oxygen in the flask before light irradiation was determined by gas chromatography (Series 400 G/C, GOW-MAC, equipped with a 5× molecular sieve column and a TC detector, and operated with argon as the carrier gas). The flask was then put into a water-jacketed beaker, and the temperature was controlled to 20 °C by a temperature controller (VWR, Model 1147P). The flask was irradiated by an 18-module LED light strip (blue, $\lambda_{max}$ = 469 nm, Creative Lighting Solutions, Product Code No. CL-FRS-1212IN-RGB) which was wrapped around the water-jacketed beaker and powered by a 12 V DC transformer. During the course of a given run, the head space pressure was monitored in real-time using data acquisition software (TRH Central, Omega Engineering Inc.). At the end of each reaction, a gas sample was taken from the head space of the flask and analyzed by GC, to determine the amount of generated hydrogen.

*2-(Pyrid-2′-yl)-8-(2″,2‴-bipyrid-6″-yl)-quinoline (**2**).* An anhydrous and anaerobic THF solution (5 mL) of 6-bromo-2,2′-bipyridine (115 mg, 0.5 mmol) was placed in an acetone/dry ice bath (−78 °C) and *n*-BuLi (2.5 M in hexane, 0.2 mL, 0.5 mmol) was added slowly and the mixture was stirred at −78 °C for 1 h. Tri-*n*-butyltin chloride (0.55 mmol) was quickly added and the mixture was kept stirring at −78 °C for 20 min and then at room temperature for another 20 min. Saturated $NH_4Cl$ solution (15 mL) was added to quench the reaction that was then extracted with EtOAC (15 mL × 3). The combined organic phases were washed with brine (20 mL × 2), dried over anhydrous $MgSO_4$, and concentrated to a dark brown oil which was dried under vacuum. The 6-(tri-*n*-butylstanyl)-2,2′-bipyridine (80% pure by $^1H$ NMR) was used for the next step without further purification. The crude stannane (**6**, 200 mg, 0.45 mmol), 8-bromo-2-(pyrid-2′-yl)quinoline (**5**, 125 mg, 0.4 mmol) and anhydrous toluene (5 mL) were mixed in a pressure tube. The mixture was degassed by


DOI: 10.1021/acs.inorgchem.5b00915
*Inorg. Chem.* 2015, 54, 7873–7884

argon for 5 min under stirring. $Pd(PPh_3)_4$ (40 mg) was then added to the solution and the mixture was degassed by argon for another 5 min before the pressure tube was sealed. The mixture was heated at 120 °C overnight. After cooling, the solvent was evaporated and the resulting black oil was dissolved in $CH_2Cl_2$ (20 mL) and washed with 2 M KF solution (15 mL × 2). The combined organic phases were dried over anhydrous $MgSO_4$ and concentrated. The crude product was purified by chromatography on alumina eluting with $CH_2Cl_2$/hexanes (1:4−1:1) to give **2** as a white solid (55 mg, 46%), mp 200−201 °C: $^1$H NMR (400 MHz, $CDCl_3$): $\delta$ 8.72 (d, $J$ = 7.2, 2H), 8.66−8.61 (m, 2H), 8.49−8.46 (m, 2H), 8.37−8.33 (m, 3H), 8.00 (t, $J$ = 6.4, 1H), 7.94 (d, $J$ = 6.0, 1H), 7.83−7.77 (m, 2H), 7.72 (dd, $J$ = 6.4, 6.4, 1H), 7.34−7.31 (m, 2H). $^{13}$C NMR (126 MHz, $CDCl_3$): $\delta$ 156.7, 156.5, 156.3, 155.5, 155.7, 149.2, 149.1, 145.3, 139.0, 137.4, 137.0, 136.9, 136.0, 131.7, 128.7, 128.7, 127.8, 126.9, 124.1, 123.7, 122.1, 121.4, 119.4, 118.6.

*8-Bromo-3,3′-dimethylene-2-(pyrid-2′-yl)quinoline (**9a**).* A mixture of 3-bromo-2-nitrobenzaldehyde (**7**, 360 mg, 1.6 mmol), iron powder (420 mg, 7.5 mmol), concentrated HCl (2 drops), EtOH (6 mL), and water (1 mL) was stirred at reflux for 1.5 h. The resulting mixture was allowed to cool and then EtOAc (25 mL) and anhydrous $MgSO_4$ were added. The solid material was removed by filtration. Evaporation of the solvents gave 2-amino-3-bromobenzaldehyde (**7**) which, without further purification, was used to react with 6,7-dihydroquinolin-8(5H)-one (**8a**, 235 mg, 1.6 mmol) in EtOH (10 mL) in the presence of KOH (50 mg) at 100 °C overnight. Evaporation the solvent afforded a crude product which was purified by chromatography on silica gel, eluting with EtOAc/hexanes (1:4) to afford **9a** as a white solid (225 mg, 45%), mp 205−206 °C. $^1$H NMR (400 MHz, $CDCl_3$): $\delta$ 8.83 (dd, $J$ = 1.6, 7.8 Hz, 1H), 8.03−8.00 (m, 2H), 7.74 (dd, $J$ = 1.2, 8.4 Hz, 1H), 7.62−7.59 (m, 1H), 7.37 (t, $J$ = 8.0 Hz, 1H), 7.3 (dd, $J$ = 4.8, 7.8 Hz, 1H), 3.21−3.18 (m, 2H), 3.07−3.03 (m, 2H). $^{13}$C NMR (126 MHz, $CDCl_3$): $\delta$ 153.4, 151.5, 149.8, 145.0, 136.1, 135.5, 134.8, 132.8, 132.7, 129.4, 127.3, 126.9, 126.0, 124.2.

*8-Bromo-3,3′-trimethylene-2-(pyrid-2′-yl)-quinoline (**9b**).* Aminoaldehyde **7** (377 mg, 1.80 mmol) and 5,6,7,8-tetrahydro-9H-cyclohepta[*b*]pyridin-9-one (**8b**, 285 mg, 1.78 mmol) were dissolved in EtOH (318 mL), a saturated solution of KOH in EtOH (0.5 mL) was added, and the solution refluxed for 19 h. After cooling, water (100 mL) and saturated aqueous $NaHCO_3$ (100 mL) were added. The aqueous layer was extracted with $CH_2Cl_2$ (3 × 35 mL), dried with $MgSO_4$, and the solvent evaporated to yield a white solid (582 mg, 99.9%). $^1$H NMR (400 MHz, $CDCl_3$): $\delta$ 8.81 (dd, $J$ = 4.8, 1.6 Hz, 1H), 8.04 (dd, $J$ = 7.4, 1.3 Hz, 1H), 8.01 (s, 1H), 7.79 (dd, $J$ = 8.1, 1.3 Hz, 1H), 7.59 (dd, $J$ = 7.6, 1.6 Hz, 1H), 7.44−7.36 (m, 1H), 7.33 (dd, $J$ = 7.6, 4.8 Hz, 1H), 2.73 (t, $J$ = 7.0 Hz, 2H), 2.59 (t, $J$ = 7.1 Hz, 2H), 2.25 (p, $J$ = 7.0 Hz, 2H). $^{13}$C NMR (126 MHz, $CDCl_3$): $\delta$ 159.4, 156.6, 148.8, 144.8, 136.6, 135.7, 135.4, 134.0, 132.8, 129.4, 127.3, 126.9, 125.7, 124.0, 31.3, 29.9, 29.6.

*8-Acetyl-3,3′-dimethylene-2-(pyrid-2′-yl)quinoline (**10a**).* A mixture of **9a** (150 mg, 0.48 mmol), tri-*n*-butyl(1-ethoxyvinyl)tin (0.86 g, 2.4 mmol), [$Pd(PPh_3)_4$] (60 mg, 0.05 mmol) and toluene (5 mL) was degassed and sealed in a pressure tube. The mixture was heated at 120 °C overnight. The solvent was evaporated and the oily residue was added to an aqueous solution of KF (1.5 g in 20 mL water). The mixture was stirred at room temperature for ∼5 min and filtered through a Celite pad. The Celite pad was washed with EtOAc and the filtrate was extracted with EtOAc. The combined organic phases were dried over anhydrous $MgSO_4$ and then the solvent was evaporated. The residue was dissolved in acetone (5 mL), to which was added 2 M HCl (1.5 mL). The mixture was stirred at room temperature overnight and then neutralized with saturated $NaHCO_3$ and extracted with EtOAc. The organic extract was dried over $MgSO_4$ and the solvent was evaporated. The residue was purified by chromatography on silica eluting with hexanes/EtOAc (4:1) to afford **10a** as an off-white solid (60 mg, 46%), mp 159−160 °C. $^1$H NMR (400 MHz, $CDCl_3$): $\delta$ 8.78 (d, $J$ = 4.0 Hz, 1H), 8.06−8.04 (m, 2H), 7.92 (d, $J$ = 6.4 Hz, 1H), 7.62 (d, $J$ = 6.8 Hz, 1H), 7.57 (dd, $J$ = 6.4, 6.0 Hz, 1H), 7.31 (dd, $J$ = 4.0, 6.4 Hz, 1H), 3.25 (s, 3H), 3.20 (m, 2H), 3.09 (m, 2H). $^{13}$C NMR (100 MHz, $CDCl_3$): $\delta$ 203.4, 152.6, 151.8, 149.6, 145.59, 139.3, 136.2, 135.6, 134.5, 132.0, 131.0, 130.3, 128.4, 126.5, 124.3, 33.5, 28.2, 28.0.

*8-Acetyl-3,3′-trimethylene-2-(pyrid-2′-yl)-quinoline (**10b**).* A mixture of **9b** (220 mg, 0.677 mmol), $Pd(PPh_3)_2Cl_2$ (72 mg, 0.10 mmol), and tri-*n*-butyl(1-ethoxyvinyl)tin (1.30 mL, 3.75 mmol) was dissolved in DMF (6 mL) in a pressure tube. The solution was purged with $N_2$ for 20 min and then heated at 80 °C for 1 d. The reaction was cooled, and solvent was evaporated. The residue was added to a solution of KF (5 g) in $H_2O$ (50 mL), and the aqueous solution was filtered through Celite, eluted with EtOAc, and extracted with EtOAc (2 × 25 mL). The combined organic extracts were dried over $MgSO_4$, and the solvent evaporated. The crude material was dissolved in acetone (10 mL) and 2 N HCl (3 mL) was added. Stirring was maintained for 20 h. The reaction was neutralized with saturated $NaHCO_3$ (50 mL), and the aqueous mixture was extracted with $CH_2Cl_2$ (2 × 25 mL), dried over $MgSO_4$, and the solvent evaporated. The crude product was purified by chromatography on silica gel using hexane-EtOAc (1:2) as the eluent. The second band afforded **10b** as a yellow solid (118 mg, 60% yield). $^1$H NMR (400 MHz, $CDCl_3$): $\delta$ 8.72 (dd, $J$ = 4.8, 1.7 Hz, 1H), 8.02 (s, 1H), 8.00 (dd, $J$ = 7.2, 1.5 Hz, 1H), 7.92 (dd, $J$ = 8.1, 1.5 Hz, 1H), 7.62−7.52 (m, 2H), 7.31 (dd, $J$ = 7.6, 4.8 Hz, 1H), 3.08 (s, 3H), 2.69 (t, $J$ = 7.0 Hz, 2H), 2.54 (t, $J$ = 7.1 Hz, 2H), 2.22 (p, $J$ = 6.9 Hz, 3H). $^{13}$C NMR (101 MHz, $CDCl_3$): $\delta$ 203.7, 158.5, 156.8, 148.5, 145.0, 139.2, 136.7, 135.4, 135.2, 133.2, 131.0, 129.9, 128.2, 126.4, 123.9, 33.5, 31.2, 29.9, 29.7.

*8-(1″,10″-Phenanthrol-2″-yl)-3,3′-dimethylene-2-(pyrid-2′-yl)-quinoline (**3**).* A mixture of 8-amino-7-quinolinecarbaldehyde (48 mg, 0.218 mmol) and **10a** (54 mg, 0.197 mmol) was dissolved in EtOH (3 mL) and a saturated solution of KOH in EtOH (10 drops) was added. The solution was refluxed for 18 h. After cooling, water (20 mL) and brine (25 mL) were added. The aqueous layer was extracted with $CH_2Cl_2$ (4 × 10 mL), dried with $MgSO_4$, and the solvent evaporated. The crude material was purified by chromatography on alumina first using EtOAc as the eluent and then, as the second band begins to elute, EtOAc-MeOH (98:2) to yield an off-white solid (69 mg, 87%), mp 245−247 °C. $^1$H NMR (500 MHz, $CDCl_3$): $\delta$ 9.26 (d, $J$ = 8.4 Hz, 1H), 9.20 (dd, $J$ = 4.3, 1.7 Hz, 1H), 8.85 (dd, $J$ = 7.2, 1.5 Hz, 1H), 8.75 (dd, $J$ = 4.7, 1.7 Hz, 1H), 8.43 (d, $J$ = 8.4 Hz, 1H), 8.24 (dd, $J$ = 8.1, 1.7 Hz, 1H), 8.07 (s, 1H), 7.88 (dd, $J$ = 8.1, 1.4 Hz, 1H), 7.87 (d, $J$ = 8.8 Hz, 1H), 7.81−7.70 (m, 2H), 7.65−7.54 (m, 2H), 7.26 (dd, $J$ = 7.6, 4.7 Hz, 1H), 3.19 (t, $J$ = 7.3 Hz, 2H), 3.05 (t, $J$ = 7.3 Hz, 2H). $^{13}$C NMR (126 MHz, $CDCl_3$): $\delta$ 157.5, 152.28, 152.25, 150.2, 149.4, 146.7, 146.1, 145.7, 138.8, 136.2, 136.1, 135.5, 135.4, 134.9, 133.0, 131.5, 128.83, 128.7, 128.5, 128.0, 127.6, 126.8, 126.1, 124.0, 122.7, 28.2, 28.0.

*8-(1″,10″-Phenanthrol-2″-yl)-3,3′-trimethylene-2-(pyrid-2′-yl)-quinoline (**4**).* Following the procedure described for **3**, 8-amino-7-quinolinecarbaldehyde (50 mg, 0.220 mmol) and **10b** (57 mg, 0.198 mmol), EtOH (3 mL) and a saturated solution of KOH in EtOH (10 drops) afforded **4** as an orange oil (71 mg, 85%). $^1$H NMR (500 MHz, $CDCl_3$): $\delta$ 9.19 (dd, $J$ = 4.3, 1.7 Hz, 1H), 9.11 (d, $J$ = 8.4 Hz, 1H), 8.78 (dd, $J$ = 7.2, 1.1 Hz, 2H), 8.75 (dd, $J$ = 4.9, 1.6 Hz, 1H), 8.34 (d, $J$ = 8.4 Hz, 1H), 8.23 (dd, $J$ = 8.0, 1.7 Hz, 1H), 8.10 (s, 1H), 7.93 (dd, $J$ = 8.1, 1.3 Hz, 1H), 7.83 (d, $J$ = 8.8 Hz, 1H), 7.81−7.72 (m, 2H), 7.59 (dd, $J$ = 8.0, 4.3 Hz, 1H), 7.56 (dd, $J$ = 7.6, 1.6 Hz, 1H), 7.29 (dd, $J$ = 7.6, 4.9 Hz, 1H), 2.74 (t, $J$ = 7.0 Hz, 2H), 2.55 (t, $J$ = 7.0 Hz, 2H), 2.25 (p, $J$ = 7.0 Hz, 2H). $^{13}$C NMR (126 MHz, $CDCl_3$): $\delta$ 158.1, 157.6, 157.2, 150.2, 148.4, 146.7, 146.2, 145.3, 138.9, 136.6, 136.1, 135.7, 135.5, 135.2, 132.8, 132.6, 128.8, 128.5, 128.4, 128.0, 127.5, 126.7, 126.1, 123.7, 122.7, 120.0, 119.5, 31.3, 30.0, 29.8.

**General Procedure for the Synthesis of Cobalt Complexes.** To a methanol solution of $CoCl_2{\cdot}6H_2O$ (0.05 M), 1 equiv ligand in $CHCl_3$ (0.05 M) was slowly added with stirring. The mixture was kept stirring overnight at room temperature and the solid precipitated gradually from the solution. If no solid precipitated, $Et_2O$ was added to precipitate the product. The precipitate was collected by filtration, washed with methanol and $CHCl_3$ and dried in air to afford a green or brown solid.

*[Co(**1**)Br$_2$].* Yield = 70%. MS (ESI): calcd. for $m/z$ = 521.98 ([Co(**1**)Br]$^+$), found $m/z$ = 522.03. Elemental Analysis: calcd. for $C_{26}H_{16}Br_2CoN_4$: C, 51.77; H, 2.67; N, 9.29; found: C, 51.27; H, 3.05; N, 9.38.



DOI: 10.1021/acs.inorgchem.5b00915
*Inorg. Chem.* 2015, 54, 7873−7884

*[Co(2)Cl$_2$]*. Yield = 52%. MS (ESI): calcd. for $m/z$ = 454.04 ([Co(**2**)Cl]$^+$), found $m/z$ = 454.10. Elemental Analysis: calcd. for $C_{24}H_{16}Cl_2CoN_4 \cdot 1.25H_2O$: C, 56.22; H, 3.64; N, 10.93; found: C, 56.26; H, 4.06; N, 11.11.

*[Co(3)(OH$_2$)Cl]Cl*. Yield = 63%. MS (ESI): calcd. for $m/z$ = 504.05 ([Co(**3**)Cl]$^+$), found $m/z$ = 504.13. Elemental Analysis: calcd. for $C_{28}H_{20}Cl_2CoN_4O \cdot 0.6CHCl_3$: C, 54.41; H, 2.98; N, 9.27; found: C, 54.51; H, 3.30; N, 8.89.

*[Co(4)Cl$_2$]*. Yield = 45%. MS (ESI): calcd. for $m/z$ = 518.07 ([Co(**4**)Cl]$^+$), found $m/z$ = 518.20. Elemental Analysis: calcd. for $C_{29}H_{20}Cl_2CoN_4 \cdot 0.8CHCl_3 \cdot 2.25\ H_2O$: C, 51.85; H, 3.69; N, 8.12; found: C, 51.45; H, 3.84; N, 8.49.

**X-ray Structure Determination.** An orange plate ([Co(**3**)(OH$_2$)Cl]Cl) of dimensions 0.14 mm × 0.08 mm × 0.02 mm and an orange rod ([Co(**2**)Cl$_2$]) of dimensions 0.06 mm × 0.02 mm × 0.01 mm were mounted on MiTeGen kapton loops in the 100(2) K nitrogen cold stream provided by an Oxford Cryosystems Cryostream 700 Plus low-temperature apparatus on the goniometer head of a Bruker D8 diffractometer equipped with an PHOTON100 CMOS detector running in shutterless mode on beamline 11.3.1 at the Advanced Light Source (Berkeley, CA). Diffraction data were collected using synchrotron radiation monochromated using silicon(111) to a wavelength of 0.7749(1) Å for both samples. An approximate full sphere of data to $2\theta_{max}$ = 67.4° and 66.2°, respectively, was collected using 1° $\omega$ scans per second for each sample. Full details of the refinement and results of the experiment can be found in Table S1 and in the cif files included in the Supporting Information.

**Theoretical Studies.** All density functional theory (DFT) calculations were carried out with the Jaguar 7.6 program package by Schrödinger LLC. For geometry optimizations, solvation energy, and frequency calculations, the local M06-L functional[50,51] was used with the LACVP** core potential and basis set. Meanwhile single-point energy corrections were performed with the M06-L functional using the LACV3P**++ basis set, which, as suggested by Martin,[52] was augmented with two f-polarization functions on the ruthenium metal center. Frequency calculations were performed on the optimized geometries to verify that the geometries correspond to minima or first-order saddle points (transition states) on the potential energy surface. The Gibbs free energies were defined according to the following equation:

$$G = E(\text{M06-L/LACV3P**++2f on Co}) + G_{solv} + \text{ZPE} + H_{298} - TS_{298} + 1.9$$

[concentration correction to the free energy of solvation from 1 M(g) → 1 M(aq) to 1 atm(g) → 1 M(aq)]. The solvation model applied was the Poisson−Boltzmann reactive field implemented in Jaguar 7.6.[53] The experimental value of −270.3 kcal/mol was used for the free energy of solvating proton at pH 0 and −274.4 kcal/mol at pH 4.[54] Equilibrium constant were estimated by $K^0 = \exp[-\Delta G^0/(RT)]$, where $\Delta G^0$ is the free energy change of the reaction. Reduction potentials were calculated as

$$E(\text{NHE}) = \frac{\Delta G_r(298\ \text{K, pH 4})}{-nF} - 4.28\ \text{V}$$

where $\Delta G_r$(298 K, pH 4) is the Gibbs free energy of the reduction reaction at pH 4 and 298 K, $n$ is the number of electrons involved, and $F$ is the Faraday constant ($F$ = 23.06 kcal/V). The value of 4.28 V for the absolute hydrogen electrode was selected based on the suggestion by Isse and Gennaro.[55]

## ■ ASSOCIATED CONTENT

### Supporting Information

X-ray crystallographic data for complex [Co(**2**)Cl$_2$] and [Co(**3**)(OH$_2$)Cl]Cl in CIF format, $^1$H and $^{13}$C NMR data, mass and UV-vis spectra, electrochemical figures, and optimized structures and their Cartesian coordinates are provided as Suporting Information. The Supporting Information is available free of charge on the ACS Publications website at DOI: 10.1021/acs.inorgchem.5b00915.

## ■ AUTHOR INFORMATION


### Corresponding Authors

*E-mail: ahlqui@kth.se.

*E-mail: thummel@uh.edu.


### Notes

The authors declare no competing financial interest.

## ■ ACKNOWLEDGMENTS

We thank the Division of Chemical Sciences, Geosciences, and Biosciences, Office of Basic Energy Sciences of the U.S. Department of Energy (Grant No. DE-FG02-07ER15888) and the Robert A. Welch Foundation (Grant No. E-621) for financial support of this work. The Advanced Light Source is supported by the Director, Office of Science, Office of Basic Energy Sciences, of the U.S. Department of Energy under Contract No. DE-AC02-05CH11231.

## ■ REFERENCES


(1) Winter, M.; Brodd, R. J. *Chem. Rev.* **2004**, *104*, 4245−4269.
(2) Song, C. *Catal. Today* **2006**, *115*, 2−32.
(3) Lewis, N. S.; Nocera, D. G. *Proc. Natl. Acad. Sci. U. S. A.* **2006**, *103*, 15729−15735.
(4) Hambourger, M.; Moore, G. F.; Kramer, D. M.; Gust, D.; Moore, A. L.; Moore, T. A. *Chem. Soc. Rev.* **2009**, *38*, 25−35.
(5) Barber, J. *Chem. Soc. Rev.* **2009**, *38*, 185−196.
(6) Alstrum-Acevedo, J. H.; Brennaman, M. K.; Meyer, T. J. *Inorg. Chem.* **2005**, *44*, 6802−6827.
(7) Swierk, J. R.; Mallouk, T. E. *Chem. Soc. Rev.* **2013**, *42*, 2357−2387.
(8) Nocera, D. G. *Acc. Chem. Res.* **2012**, *45*, 767−776.
(9) Tran, P. D.; Artero, V.; Fontecave, M. *Energy Environ. Sci.* **2010**, *3*, 727−747.
(10) Sakai, K.; Ozawa, H. *Coord. Chem. Rev.* **2007**, *251*, 2753−2766.
(11) Du, P.; Schneider, J.; Jarosz, P.; Eisenberg, R. *J. Am. Chem. Soc.* **2006**, *128*, 7726−7727.
(12) Heyduk, A. F.; Nocera, D. G. *Science* **2001**, *293*, 1639−1641.
(13) Dubois, D. L. *Inorg. Chem.* **2014**, *53*, 3935−3960.
(14) Tard, C.; Pickett, C. J. *Chem. Rev.* **2009**, *109*, 2245−2274.
(15) Thoi, V. S.; Sun, Y.; Long, J. R.; Chang, C. J. *Chem. Soc. Rev.* **2013**, *42*, 2388−2400.
(16) Artero, V.; Chavarot-Kerlidou, M.; Fontecave, M. *Angew. Chem., Int. Ed.* **2011**, *50*, 7238−7266.
(17) Eckenhoff, W. T.; Eisenberg, R. *Dalton Trans.* **2012**, *41*, 13004−13021.
(18) Sun, Y.; Bigi, J. P.; Piro, N. a; Tang, M. L.; Long, J. R.; Chang, C. J. *J. Am. Chem. Soc.* **2011**, *133*, 9212−9215.
(19) Nippe, M.; Khnayzer, R. S.; Panetier, J. a.; Zee, D. Z.; Olaiya, B. S.; Head-Gordon, M.; Chang, C. J.; Castellano, F. N.; Long, J. R. *Chem. Sci.* **2013**, *4*, 3934−3945.
(20) Khnayzer, R. S.; Thoi, V. S.; Nippe, M.; King, A. E.; Jurss, J. W.; El Roz, K. A.; Long, J. R.; Chang, C. J.; Castellano, F. N. *Energy Environ. Sci.* **2014**, *7*, 1477−1488.
(21) Singh, W. M.; Baine, T.; Kudo, S.; Tian, S.; Ma, X. A. N.; Zhou, H.; DeYonker, N. J.; Pham, T. C.; Bollinger, J. C.; Baker, D. L.; Yan, B.; Webster, C. E.; Zhao, X. *Angew. Chem., Int. Ed.* **2012**, *51*, 5941−5944.
(22) Call, A.; Codolà, Z.; Acuña-Parés, F.; Lloret-Fillol, J. *Chem. - Eur. J.* **2014**, *20*, 6171−6183.
(23) Kawano, K.; Yamauchi, K.; Sakai, K. *Chem. Commun.* **2014**, *50*, 9872−9875.
(24) Connolly, P.; Espenson, J. H. *Inorg. Chem.* **1986**, *25*, 2684−2688.




DOI: 10.1021/acs.inorgchem.5b00915
*Inorg. Chem.* 2015, 54, 7873−7884

(25) Baffert, C.; Artero, V.; Fontecave, M. *Inorg. Chem.* **2007**, *46*, 1817−1824.
(26) Jacques, P.-A.; Artero, V.; Pécaut, J.; Fontecave, M. *Proc. Natl. Acad. Sci. U. S. A.* **2009**, *106*, 20627−20632.
(27) Stubbert, B. D.; Peters, J. C.; Gray, H. B. *J. Am. Chem. Soc.* **2011**, *133*, 18070−18073.
(28) Hu, X.; Brunschwig, B. S.; Peters, J. C. *J. Am. Chem. Soc.* **2007**, *129*, 8988−8998.
(29) McCrory, C. C. L.; Uyeda, C.; Peters, J. C. *J. Am. Chem. Soc.* **2012**, *134*, 3164−3170.
(30) Du, P.; Schneider, J.; Luo, G.; Brennessel, W. W.; Eisenberg, R. *Inorg. Chem.* **2009**, *48*, 4952−4962.
(31) Krishnan, C. V.; Sutin, N. *J. Am. Chem. Soc.* **1981**, *103*, 2141−2142.
(32) Creutz, C.; Sutin, N. *Coord. Chem. Rev.* **1985**, *64*, 321−341.
(33) Goldsmith, J. I.; Hudson, W. R.; Lowry, M. S.; Anderson, T. H.; Bernhard, S. *J. Am. Chem. Soc.* **2005**, *127*, 7502−7510.
(34) Schwarz, H. A.; Creutz, C.; Sutin, N. *Inorg. Chem.* **1985**, *24*, 433−439.
(35) Bigi, J. P.; Hanna, T. E.; Harman, W. H.; Chang, A.; Chang, C. J. *Chem. Commun.* **2010**, *46*, 958−960.
(36) Leung, C.-F.; Ng, S.-M.; Ko, C.-C.; Man, W.-L.; Wu, J.; Chen, L.; Lau, T.-C. *Energy Environ. Sci.* **2012**, *5*, 7903−7907.
(37) Tong, L.; Zong, R.; Thummel, R. P. *J. Am. Chem. Soc.* **2014**, *136*, 4881−4884.
(38) Morosin, B. *J. Chem. Phys.* **1966**, *44*, 252−257.
(39) Pagola, S.; Trowell, K. T.; Havas, K. C.; Reed, Z. D.; Chan, D. G.; Van Dongen, M. J.; DeFotis, G. C. *Inorg. Chem.* **2013**, *52*, 13341−13350.
(40) Brown, G. M.; Brunschwig, B. S.; Creutz, C.; Endicott, J. F.; Sutin, N. *J. Am. Chem. Soc.* **1979**, *101*, 1298−1300.
(41) Han, Z.; Qiu, F.; Eisenberg, R.; Holland, P. L.; Krauss, T. D. *Science* **2012**, *338*, 1321−1324.
(42) Hoffert, W. A.; Roberts, J. A.; Bullock, R. M.; Helm, M. L. *Chem. Commun.* **2013**, *49*, 7767−7769.
(43) The uncertainties in the dimerization process are, however, relatively high, since we cannot assume error cancellation in the solvation model when two species interact.
(44) Tong, L.; Duan, L.; Xu, Y.; Privalov, T.; Sun, L. *Angew. Chem., Int. Ed.* **2011**, *50*, 445−449.
(45) Diedrich, C. L.; Haase, D.; Christoffers, J. *Synthesis* **2008**, *2008*, 2199−2210.
(46) Riesgo, E. C.; Jin, X.; Thummel, R. P. *J. Org. Chem.* **1996**, *61*, 3017−3022.
(47) Thummel, R. P.; Lefoulon, F.; Cantu, D.; Mahadevan, R. *J. Org. Chem.* **1984**, *49*, 2208−2212.
(48) Kanan, M. W.; Nocera, D. G. *Science* **2008**, *321*, 1072−1075.
(49) Connelly, N. G.; Geiger, W. E. *Chem. Rev.* **1996**, *96*, 877−910.
(50) Zhao, Y.; Truhlar, D. G. *J. Chem. Phys.* **2006**, *125*, 194101−194118.
(51) Ertem, M. Z.; Cramer, C. J. *Dalton Trans.* **2012**, *41*, 12213−12219.
(52) Martin, J. M. L.; Sundermann, A. *J. Chem. Phys.* **2001**, *114*, 3408−3420.
(53) Marten, B.; Kim, K.; Cortis, C.; Friesner, R. A.; Murphy, R. B.; Ringnalda, M. N.; Sitkoff, D.; Honig, B. *J. Phys. Chem.* **1996**, *100*, 11775−11788.
(54) Tissandier, M. D.; Cowen, K. A.; Feng, W. Y.; Gundlach, E.; Cohen, M. H.; Earhart, A. D.; Coe, J. V.; Tuttle, T. R. *J. Phys. Chem. A* **1998**, *102*, 7787−7794.
(55) Isse, A. A.; Gennaro, A. *J. Phys. Chem. B* **2010**, *114*, 7894−7899.



DOI: 10.1021/acs.inorgchem.5b00915
*Inorg. Chem.* 2015, 54, 7873−7884